Preprint (LBNL Reports) - submitted to Physica Status Solidi (b) (2008)

Femtosecond THz Studies of Intra-Excitonic Transitions

Rupert Huber, Ben A. Schmid, Robert A. Kaindl, and Daniel S. Chemla

Department of Physics, University of California at Berkeley and Materials Sciences Division, E. O. Lawrence Berkeley National Laboratory, 1 Cyclotron Road, Berkeley, CA 94720, USA

Abstract:

Few-cycle THz pulses are employed to resonantly access the internal fine structure of photogenerated excitons in semiconductors, on the femtosecond time scale. This technique allows us to gain novel insight into many-body effects of excitons and reveal key quantum optical processes. We discuss experiments that monitor the density-dependent renormalization of the binding energy of a high-density exciton gas in GaAs/$Al_{0.3}Ga_{0.7}As$ quantum wells close to the Mott transition. In a dilute ensemble of 3p excitons in Cu_2O, stimulated THz emission from internal transitions to the energetically lower 2s state is observed at a photon energy of 6.6 meV, with a cross section of 10^{-14} cm^2. Simultaneous interband excitation of both exciton levels drives quantum beats, which cause efficient THz emission at the difference frequency. By extending this principle to various other exciton resonances, we develop a novel way of mapping the fine structure by two-dimensional THz emission spectroscopy.

1. Introduction

In the dilute limit, excitons in semiconductors may be regarded as Coulomb-bound quasi-particles of a conduction electron with a defect electron (hole) [1,2]. Starting with the quantized internal fine structure, there is a wealth of compelling analogies to atoms. This has motivated research aimed at using excitons as tailorable model systems for atomic gases, potentially implying the perspective of novel quantum collective states of excitons [3].

Nevertheless, there are limits to the atomic analogy. Electron-hole pairs are inherently unstable due to ultrafast recombination. Due to efficient dielectric screening and low effective masses of charge carriers in semiconductors, excitons feature typical binding energies in the meV range, orders of magnitude lower than the atomic Rydberg constant. As complex many-body states embedded in a crystal lattice, excitons strongly interact with lattice vibrations, other excitons, as well as charge carriers. Depending on excitation density and temperature, intriguing new phases may occur. Such phenomena range from molecule-like complexes such as biexcitons via the exciton Mott transition [4,5], to the highly controversially discussed Bose Einstein condensation (BEC) [6-8].

Up to now, most experiments that are targeted to unravel the interplay of these phenomena have studied interband resonances in the visible and infrared spectral range. Since these techniques monitor the creation or annihilation of electron-hole pairs, they are only indirectly sensitive to existing exciton populations [9]. Moreover, they are subject to additional selection rules and often detect only a subset of excitons with vanishing center-of-mass momenta. In particular, promising systems for potential BEC of

excitons couple only weakly to radiative interband transitions. A lively discussion has been centered on the interpretation of optical spectroscopy [5,8-11].

In contrast, femtosecond terahertz (THz) technology (1 THz ≈ 4.1 meV) has been advanced in recent years to directly trace low-energy excitations in non-equilibrium electron-hole systems [12-18]. Via few-cycle THz pulses one may couple resonantly to internal exciton transitions [12,15,17,18] to explore novel quantum optical processes and shed new light on the complex phase diagram of electron-hole excitations in semiconductors.

In the following section, we briefly review the state of the art of broadband and ultrabroadband THz technology. These tools are then exploited to study a two-dimensional exciton gas at high densities close to the Mott criterion [17], as discussed in section 3. The THz data provide direct insight into the many-body renormalization of the exciton fine structure. In section 4, a novel analogy between atoms and excitons is discussed: the first observation of stimulated emission of electromagnetic radiation from intra-excitonic transitions [18]. Section 5 reports a new approach to intra-excitonic spectroscopy based on THz generation by inter-level quantum beats.

2. Optical pump – THz probe experiments

The experimental scheme employed in this work is optical pump – THz probe spectroscopy: A first spectrally shaped femtosecond pulse in the visible or near-infrared domain generates excitons or unbound electron-hole pairs via an interband absorption process. A subsequent ultrashort THz pulse probes the internal response of the bound *e-h* pairs with femtosecond temporal resolution.

In recent years, a variety of techniques for generating ultrashort THz transients has been developed [20]. We employ optical rectification of intense near-infrared laser pulses in nonlinear optical crystals as a particularly versatile approach: Difference frequency generation within the broad spectrum of a single femtosecond light pulse yields inherently phase-locked electromagnetic waves. While the idea was initially exploited for far-infrared transients with frequencies typically up to a few THz, recent years have seen a rapid extension towards the near-infrared domain. Ever shorter pump pulses, efficient and tuneable phase-matching schemes [21,22], and a variety of crystal materials with high $\chi^{(2)}$ nonlinearities, such as ZnTe, GaP, GaSe, or $LiIO_3$, have enabled this vast progress [20-24]. Fig. 1(d) displays selected THz spectra covering the far- and mid-infrared, as obtained by a variety of pump spectra and emitter crystals described in the figure caption. Phase matched optical rectification of 7 fs visible light pulses in a thin birefringent $LiIO_3$ emitter very recently enabled multi-THz spectra spanning beyond an optical octave, with center frequencies of up to 100 THz (photon energy > 400 meV) [curve (*iv*) of Fig. 1(d)] [24]. New perspectives open up by the possibilities to generate THz pulses with MV/cm peak electric fields in a broad range and precisely shape the wave form of multi-THz field transients [25,26].

Much of the uniqueness of THz spectroscopy arises from the availability of amplitude- and phase-sensitive detectors, recording the real-time evolution of the oscillating electric field of the infrared pulses [Fig. 1(a)-(c)]. Free-space electro-optic sensing [27] has now been advanced to measure electromagnetic field transients with frequency components ranging from 100 GHz to beyond 100 THz [28,22,23] (see Fig. 1). The spectral window accessible with phase-locked generation and field-resolved

detection of THz pulses thus now covers exciton binding energies of virtually all relevant semiconductors.

In the pump-probe experiment, a well-defined THz field transient is propagated through the semiconductor sample. By electro-optic detection, we characterize both the reference field E_{THz} transmitted through the sample in equilibrium (no excitons present) and its pump-induced change ΔE_{THz} after a fixed pump-probe delay time Δt, with amplitude and phase. From this information, the entire complex-valued optical conductivity $\sigma(\omega)$ and its transient change $\Delta\sigma(\omega,\Delta t)$ are obtained as a function of the delay time Δt [29,14-18]. The retrieval algorithm accounts for the precise sample geometry via a transfer matrix formalism [19]. The full THz dielectric response may be written as $\sigma(\omega) = \sigma_1(\omega) - i\omega\varepsilon_0(1-\varepsilon_1(\omega))$. The real part of the optical conductivity $\sigma_1(\omega)$ is a measure of the absorbed power density, while the real part of the dielectric function $\varepsilon_1(\omega)$ provides a measure of the out-of-phase, inductive response. In the following sections, we will discuss optical pump – THz probe experiments that reveal novel analogies of excitons and atoms as well as important limitations of this picture.

3. THz study of a high-density exciton gas in GaAs quantum wells

A particularly intriguing region of the phase diagram of electron-hole systems in semiconductors is given by the high-density limit of exciton gases close to the so-called Mott transition [1,2,4,5]: Charge-neutral excitons, whose ground state excitation is the transition from 1s to 2p levels, form at sufficiently low densities and temperatures. With increasing densities these bound states are distinctly modified due to many-body effects,

ultimately depleting the population of bound states. The system then undergoes a crossover into a conductive phase with a continuous low-energy excitation spectrum. In contrast to indirect interband probes, THz pulses resonantly monitor the characteristic low-energy spectra, providing an immediate measure of binding energies, as the system approaches the Mott transition.

Quasi-2D excitons in quantum wells are particularly well-suited for these investigations, owing to enhanced excitonic binding and sharp optical resonances [30]. Our sample consists of a stack of ten undoped 14-nm-wide GaAs wells separated by 10-nm-wide $Al_{0.3}Ga_{0.7}As$ barriers. The near infrared absorption spectrum [Fig. 2(a)] is dominated by the 1s heavy-hole (1sHH) exciton line at 1.540 eV. Its linewidth of 0.8 meV (FWHM) attests to a high sample quality. With increasing energy the 2s heavy-hole, the 1s light-hole exciton, and the band-to-band continuum follow. The near-infrared excitation spectrum [dotted curve, Fig. 1(a)] is tuned to resonantly generate 1s excitons.

Fig. 2 displays photo-induced THz conductivity spectra $\Delta\sigma_1(\omega)$ and dielectric function changes $\Delta\varepsilon_1(\omega)$ at a delay time Δt = 2.5 ps after near-infrared excitation. For the lowest density of $n = 2 \times 10^{10}$ cm^{-2}, a narrow asymmetric peak in $\Delta\sigma_1(\omega)$ at $\hbar\omega$ = 7 meV witnesses the existence of bound *e-h* pairs. The maximum arises from the transition from 1s to 2p quantum states, while the high-energy shoulder corresponds to transitions from 1s into higher bound and continuum states. The conductivity vanishes at low frequencies, confirming the insulating nature of the dilute gas. The dispersive zero crossing of $\Delta\varepsilon_1$ at $\hbar\omega$ = 7 meV is characteristic of the intra-excitonic oscillator.

With increasing pump density, profound changes occur in the THz response of Fig. 2: (*i*) The area enclosed by the conductivity curve $\Delta\sigma_1(\omega)$, i.e. the oscillator strength in the THz window, increases. (*ii*) The observed THz resonance strongly broadens. (*iii*) Both the spectral maximum of $\Delta\sigma_1(\omega)$ and the zero crossing of $\Delta\varepsilon_1(\omega)$ shift to lower frequencies. At the highest experimentally demonstrated density, the conductivity rises monotonically towards lower frequencies and a zero crossing of the dielectric function is not detected. This behavior indicates a conductive phase in the absence of excitonic resonances.

For a first-order analysis, we model the experimentally determined THz response (Fig. 2) via the straightforward dielectric function of two-dimensional excitons

$$\varepsilon_X(\omega) = \varepsilon_\infty + \frac{n_X e^2}{\varepsilon_0 m} \sum_q \frac{f_{1s,q}}{(\omega_{1s,q}^2 - \omega^2) - i\omega\Gamma_X} \qquad (1)$$

where ε_∞ and ε_0 are the background and vacuum dielectric constants, respectively, and *e* and *m* are elementary charge and the reduced exciton mass. The oscillator strengths for internal transitions from 1s to higher bound and unbound states are calculated from two-dimensional exciton wave functions [2,31]. We vary the exciton density n_X, the energy position $E_{1s\text{-}2p} = \hbar\omega_{1s,2p}$, and the phenomenological exciton broadening parameter Γ_X to fit the measured conductivity curves. While agreement is good for low densities, at elevated pump powers Eq. (1) does not reproduce both conductivity and dielectric function changes simultaneously (cf. broken curve in Fig. 2). This problem may be resolved by considering additional low-frequency spectral weight in the form of a coexisting plasma

of unbound *e-h* pairs. We approximate the response of this two-component system by adding a Drude term to the dielectric function of Eq. (1)

$$\varepsilon(\omega) = \varepsilon_X + \frac{n_{eh} e^2}{\varepsilon_0 m} \frac{1}{\omega^2 - i\omega\Gamma_D} \qquad (2)$$

with the density of unbound pairs n_{eh}, and a phenomenological scattering rate Γ_D. With this correction, excellent agreement with the experiment is obtained for both functions $\Delta\sigma_1(\omega)$ and $\Delta\varepsilon_1(\omega)$ at all densities and throughout the broad THz frequency band (Fig. 2).

The resulting fit parameters are depicted in Figure 3. Part (a) shows a strong saturation of the total electron-hole pair density $n = n_X + n_{eh}$ as a function of the pump power, as expected due to bleaching of the near-infrared 1s heavy-hole line. According to our model, for densities below $n = 5 \times 10^{10}$ cm^{-2}, mainly excitons are generated. With n increasing, the population share of unbound carriers becomes more prominent. Beyond a critical density $n_C = 2 \times 10^{11}$ cm^{-2}, photoexcitation creates primarily unbound *e-h* pairs. An excitonic resonance is absent and the THz response can be fully explained by the Drude model.

Most importantly, the renormalization of the excitonic fine structure with increasing photoexcitation is quantitatively described via the resonance frequency $E_{1s\text{-}2p}$ and the broadening parameter $\Gamma_{1s\text{-}2p}$ [see Fig. 3(c) and (d), respectively]. The curves reveal a strong monotonous redshift and broadening of the THz resonance.

Density-dependent many-body interactions also renormalize the near-infrared interband resonance [32]. For comparison with the THz data, open circles in Fig. 3(c) indicate the energy shift of the near-infrared 1sHH resonance. Since the net blue shift is

comprised of an elusive combination of several counteracting effects, such as band gap renormalization, phase-space filling and screening, its interpretation requires sophisticated model assumptions. In contrast, the intra-excitonic transitions observed at THz frequencies are unaffected by band-gap shifts and directly gauge the weakening of the binding energy.

Fig. 3(d) compares the density-dependent broadening Γ_{NIR} of the near-infrared 1sHH absorption line with Γ_{THz}. Remarkably, broadening of the THz response is about four times larger. We suggest that this finding results from enhanced sensitivity of the 2*p* exciton, not visible in near-infrared spectra, to screening and scattering: its radial extent (expectation value $\langle r_{2p} \rangle$ = 58 nm, obtained from our exciton model in the dilute limit) is six times that of 1s excitons. The combination of near-infrared and THz probes allows for a first direct observation of this enhancement.

The experimental accessibility of the complex broadband response function imposes strict limits on the model description. The above phenomenological two component model thus reproduces the THz data remarkably well. Quantum many-body theories have addressed the higher-order interplay of excitons with unbound *e*-*h* pairs [1,33]. We anticipate that our studies will stimulate further developments and quantitative comparison between the THz response and many-body theories of *e*-*h* gases.

4. Stimulated THz emission from internal exciton transitions in Cu_2O

So far, we have studied absorption of THz photons promoting ground state excitons into higher bound energy levels. Theoretical work suggests how the underlying elementary

processes may be effectively reversed to induce THz gain from inverted exciton populations [34,35]. Yet, stimulated emission of THz radiation connecting internal exciton levels had not been observed experimentally. One of the main complications comes from efficient non-radiative processes, such as scattering with phonons, excitons and free carriers, which lead to ultrafast relaxation to the lowest bound exciton level. These processes and THz absorption into higher bound and continuum states compete with stimulated emission and are not well understood.

Here, we show that few-cycle THz probe pulses provide the necessary time resolution to unravel the ultrafast dynamics of such processes. We discuss experiments that have observed the first stimulated emission of electromagnetic radiation from internal excitonic transitions [18]. The far-infrared response of the semiconductor Cu_2O is monitored upon resonant generation of 3p excitons. Stimulated emission from the 3p to the energetically lower 2s level manifests itself by a negative change of the absorption coefficient at a photon energy of 6.6 meV.

The semiconductor Cu_2O forms a particularly well-defined laboratory for these experiments. Since excitons in Cu_2O are counted among the most serious candidates for Bose Einstein condensation [8], the system has been extensively investigated by photoluminescence [8], Raman [36], mid-infrared [37], and high-resolution spectroscopy [38]. The visible absorption spectrum of our 330-μm-thick, naturally grown single-crystal is dominated by a series of sharp lines originating from the 2p, 3p, 4p, and 5p excitons of the yellow series, below the pair continuum (see Fig. 4). Due to the positive parity of the valence and conduction band minima at the Brillouin zone center, even parity s and d

excitons are dipole forbidden [39]. Figure 4(a) shows a detailed exciton term scheme, with the energy difference to the 3p level given on the left.

An ultrafast Ti:sapphire regenerative amplifier provides 42-fs light pulses at a center wavelength of 800 nm and a repetition rate of 250 kHz. These pulses simultaneously serve as the pump for an optical parametric amplifier (OPA) and drive optical rectification and electro-optic sampling in 500-μm-thick ZnTe elements. Near-bandwidth-limited light pulses tunable around a wavelength of 575 nm (corresponding to a photon energy of 2.16 eV) are obtained from the OPA and a subsequent pulse shaper.

We selectively excite the Cu_2O sample either resonantly at specific exciton lines or in the pair continuum and follow the subsequent transient changes in the THz response. A typical pump spectrum is indicated by the dashed curve in Fig. 4. Part (b) and (c) show the transmitted probe field $E_{\mathrm{THz}}(t)$ without photoexcitation (gray lines, downscaled by a factor of 500), and its transient change $\Delta E_{\mathrm{THz}}(\Delta t,t)$ induced by optical pumping at two different wavelengths. The time delay between the yellow pump and the electro-optic gating pulse is kept fixed at Δt = 1 ps. The response reveals critical wavelength dependence: Excitation in the continuum [Fig. 4(b)] induces electric field transients that resemble the reference pulse with a phase offset. In contrast resonant excitation of 3p excitons shows a markedly different shape of the induced field. In particular, we find a striking phase shift by π [see blue arrow in Fig. 4(c)]. We will see below that this unusual field trace is a fingerprint of stimulated THz emission.

It is illuminative for these experiments to discuss instead of the complex THz conductivity a derived quantity: the pump-induced change $\Delta\tilde{n}(\omega) = \Delta n(\omega) + i(c/2\omega)\Delta\alpha(\omega)$

of the complex refractive index. Here Δn denotes the differential change of the real part of the refractive index and $\Delta\alpha$ the absorption change. Figure 5 displays Δn and $\Delta\alpha$ obtained from the traces in Fig. 4. Continuum excitation [Figs. 5 (a),(b)] results in a predominantly inductive THz response, well explained by the Drude theory (dashed-dotted lines) of a conducting *e-h* gas. In contrast, selective excitation of the 3p interband resonance yields a pronounced spectral structure in both $\Delta\alpha$ and Δn. With increasing frequency, a peak of enhanced absorption occurs at 4.5 meV, followed by a narrow minimum of $\Delta\alpha$ at 6.6 meV [Fig. 5 (d)]. Indeed, here the induced absorption becomes negative. Δn [Fig. 5 (c)] displays a steep negative slope at a frequency of 4.5 meV, characteristic of a strong absorption line. In contrast, the dispersion of Δn at the THz photon energy of 6.6 meV has an anomalous positive gradient.

These findings consistently identify the negative absorption peak as stimulated THz emission via the 3p→2s intra-excitonic transition. This conclusion is further substantiated by the following three key observations: (*i*) unexcited Cu_2O shows no discernible THz absorption in this frequency range, (*ii*) the minimum with $\Delta\alpha < 0$ appears exclusively after resonant excitation of 3p excitons, and (*iii*) the observed resonance energy of 6.6 meV is precisely identical with the 3p–2s level spacing (Fig. 4).

For further analysis, we model the lineshape of the THz response upon 3p excitation. An accurate representation of the experiment is achieved with a model of three oscillators [dashed lines, Figs. 5 (c), (d)]. By comparison with the term scheme of Fig. 4 we attribute the lowest-frequency oscillator centered at 4.5 meV to the joint effects of 3p-4s and 3p-4d transitions. The center oscillator at 6.6 meV exhibits negative oscillator strength, in accordance with the 3p-2s stimulated emission. Finally, the component at 9.5

meV phenomenologically describes all transitions to higher bound states. The relative oscillator strengths $f_1:f_2:f_3 = 2.7:(-1):1.1$ agree qualitatively with a hydrogen model [4.3:(-1):2], thus supporting this assignment [40]. A more rigorous theory should also take into account the partial d-character of the 2s exciton in Cu_2O, as described in Ref. [39]. With an estimated density of 3p excitons of 3×10^{13} cm^{-3} we obtain a gain cross section for the 3p→2s transition of $\sigma \sim 10^{-14}$ cm^2, well in line with order-of-magnitude estimates based on hydrogen-like exciton wave functions [34].

Observation of stimulated THz emission critically depends on a high temporal resolution, as seen in Fig. 5(e). The induced response of electron-hole pairs is shown to exponentially decay increasingly faster as we turn from unbound states (τ = 36 ps), via the 3p (τ = 1.3 ps) to the 2p exciton (τ = 0.8 ps). The relative spectral shape does not vary strongly in time (not shown). The respective relaxation times are explained by recombination and scattering of excitons into the long-lived 1s state mediated by optical phonon interactions [36] and confirm the assignment of the THz resonances.

5. THz generation by exciton quantum beats

Under modified excitation conditions, coherent quantum beats of 3p and 2s states lead to THz generation even without stimulation by external THz fields. For this set of experiments, the pump spectrum is tuned and broadened to overlap simultaneously the 3p and the dipole-forbidden 2s resonances [Fig. 6(a)]. No THz probe light is incident on the sample.

We observe emission of a coherent THz field shown in Fig. 6(b). The transient is detected electro-optically by scanning the delay Δt between the visible pump and the gating pulse. The corresponding power spectrum in Fig. 6(c) peaks at 6.6 meV and exhibits a width of 1.7 meV (FWHM). This lineshape coincides with the values deduced from the 3p-2s transition in Fig. 5(d), corroborating that the THz transient originates from the same internal exciton transition. The absolute size of these emitted fields is comparable to the transients ΔE_{THz} in Fig. 4 stimulated by a far-infrared seed pulse. This fact implies that the generation mechanism cannot be explained by a spontaneous version of the gain process discussed above. Moreover, we find that the THz polarization is parallel to the linear polarization of the pump light, whereas the polarization of the stimulated change ΔE_{THz}, described further above, is determined by the probe pulses.

We interpret this THz emission as resulting from quantum beats between coherent exciton polarizations. Visible light induces 3p exciton polarizations, while the low-energy wing of the pump spectrum couples the 2s level to the ground state, e.g. via a weak quadrupole or surface field assisted dipole transition [34]. As 3p and 2s states possess opposite parity, quantum beats between them act as a radiating dipole. The THz generation may be expressed as an effective difference frequency process (see insert of Fig. 6), described by the nonlinear susceptibility

$$\chi_{eff}^{(2)}(\omega) \propto \frac{M_{3p} M_{2s} M_{3p-2s}}{\left(\omega - \omega_{3p} + i\Gamma_{3p}\right)\left(\omega_{THz} - \omega_{3p-2s} + i\Gamma_{3p-2s}\right)} \qquad (3)$$

where $M_{3\mathrm{p}}$ and $M_{2\mathrm{s}}$ are the visible interband matrix elements, $M_{3\mathrm{p}\text{-}2\mathrm{s}}$ is the THz dipole matrix element. ω and ω_{THz} are the frequencies of visible pump and emitted THz fields,

and ω_{3p} and $\omega_{3p\text{-}2s}$ are visible 3p and THz 3p-2s resonance energies with corresponding dephasing constants Γ_i. Equation (3) follows from a simplified treatment of stimulated polariton scattering [41].

In our experiment, one of the denominator terms is chosen resonant by the pump photon energy ($\omega = \omega_{3p}$), and THz emission is observed whenever $\omega_{THz} = \omega_{3p\text{-}2s}$. For this THz frequency both terms in the denominator are resonant, overcoming the weakness of the coupling between 2s excitons and the ground state. Off-resonant pumping reduces the conversion efficiency strongly as demonstrated below. The emitted THz intensity scales with the square of the pump power (not shown) characteristic of a $\chi^{(2)}$ effect. From the pulse intensities and effective interaction length we estimate a resonant nonlinearity of $\chi_{eff}^{(2)} \geq 10$ pm/V. This value exceeds the high background nonlinearity of non-centrosymmetric materials such as ZnTe, which is widely used for THz generation [28].

The above principle of THz emission may be extended to map out the internal fine structure of excitons in a systematic way. By detuning the pump spectra from the one depicted in Fig. 6(a), one may induce a coherent superposition of various alternative pairs of excitonic quantum states. This idea is implemented in Fig. 7. The power spectra of the emitted THz radiation exhibits a resonant enhancement of $\chi^{(2)}$ whenever a pair of exciton states of opposite parity is excited: The THz spectrum of Fig. 6 is reproduced for a pump spectrum centered at 2.158 eV [see also Fig. 6(a)] due to coherent quantum beats of 2s and 3p excitons. At lower pump photon energies, THz emission becomes inefficient and spectrally less selective as expected from Eq. (3), since the resonance denominator is no longer singular. On the other hand, if the pump photons have sufficient energy to drive alternative pairs of excitonic states, such as (4p, 3s) or (4p, 3d), $\chi^{(2)}$ is resonantly

enhanced at the corresponding THz photon energies. In fact, the spectra of Fig. 7 clearly reflect this situation for intra-excitonic transitions 3p-2s, 4p-3s, and 4p-3d. Interestingly, THz generation is most efficient for the 3p-2s quantum beat. This observation may be explained by the relative size of the matrix elements M_i which are expected to decrease rapidly with increasing principal quantum number [2]. Our novel spectroscopy scheme may become a helpful tool to systematically map out the internal fine structure of excitons also in other semiconductor systems.

6. Conclusion

We have used broadband THz spectroscopy to study the ultrafast dynamics, spectral positions, widths and oscillator strengths of intra-excitonic transitions. In a two-dimensional exciton gas in GaAs quantum wells, the density-dependent renormalization of the excitonic fine structure was directly recorded by probing the THz absorption from the 1s-2p transition. Furthermore, we have demonstrated the inverse quantum process, stimulated THz emission between the 3p and 2s exciton states in Cu_2O with a significantly large cross section. This underpins the analogy between excitons and atoms. A novel intra-excitonic quantum beat spectroscopy, finally, allows us to map out an extended set of transitions between several excited states. While the experiments discussed here focus on far-infrared exciton lines, latest advances in ultra-broadband nonlinear optics pave the way for THz studies of more strongly bound systems with high thermal stability.

The experiments yield novel insight into the complex phase diagram of excitons and provide access to key quantum optical processes. These are key ingredients for future

THz quantum optical manipulations of excitons outside the optically accessible range. Hence, THz opto-electronics may become a helpful tool in the ongoing quest for excitonic Bose Einstein condensation.

Acknowledgements.

We thank Y. R. Shen, C. Kübler, A. Leitenstorfer, N. C. Nielsen, and T. Zentgraf for helpful discussions and continuous support. J. Reno is acknowledged for providing quantum-well samples. This work was supported by the Director, Office of Science, Office of Basic Energy Science of the US Department of Energy under Contract No. DE-AC02-05CH11231. R.H. is grateful for support from the Alexander von Humboldt Foundation and the German Research Foundation through the Emmy Noether Program.

References

1. R. Zimmermann, Many-Particle Theory of Highly Excited Semiconductors, Teubner-Texte zur Physik, Vol. **18** (BSB Teubner, Berlin, 1987).
2. H. Haug and S. W. Koch, Quantum Theory of the Optical and Electronic Properties of Semiconductors (World Scientific, Singapore, 2004).
3. I. Perakis, Nature **417**, 33 (2002) and references therein.
4. N.F. Mott, Metal Insulator Transitions (Taylor and Francis, London, 1990).
5. L. Kappei, J. Szczytko, F. Morier-Genoud, B. Deveaud, Phys. Rev. Lett. **94**, 147403 (2005).
6. L.V. Butov, C.W. Lai, A.L. Ivanov, A.C. Gossard, D.S. Chemla, Nature **417**, 47 (2002); L.S. Levitov, B.D. Simons, L.V. Butov, Phys. Rev. Lett. **94**, 176404 (2005).
7. D. Snoke, S. Denev, Y. Liu, L. Pfeiffer, K. West, Nature **418**, 754 (2002).
8. D. W. Snoke, J.P. Wolfe, A. Mysyrowicz, Phys. Rev. Lett. **64**, 2543 (1990); K.E. O'Hara, J.P. Wolfe, Phys. Rev. B **62**, 12909 (2000).
9. M. Kira, W. Hoyer, T. Stroucken, S.W. Koch, Phys. Rev. Lett. **87**, 176401 (2001).
10. J. Szczytko, et al., Phys. Rev. Lett. **93**, 137401 (2004); Phys. Rev. B **71**, 195313 (2005).
11. S. Chatterjee et al., Phys. Rev. Lett. **92**, 067402 (2004).
12. R.H.M. Groeneveld, D. Grischkowsky, J. Opt. Soc. Am. B **11**, 2502-2507 (1994).
13. J. Cerne, J. Kono, M.S. Sherwin, M. Sundaram, A.C. Gossard, G.E.W. Bauer, Phys. Rev. Lett. **77**, 1131 (1996).
14. R. Huber, F. Tauser, A. Brodschelm, M. Bichler, G. Abstreiter and A. Leitenstorfer, Nature **414**, 286 (2001).
15. R.A. Kaindl, M.A. Carnahan, D. Hägele, R. Lövenich, D.S. Chemla, Nature **423**, 734 (2003).
16. R. Huber, et al., Phys. Rev. Lett. **94**, 027401 (2005).
17. R. Huber, R. A. Kaindl, B. A. Schmid, and D. S. Chemla, Phys. Rev. B. **72**, 161314(R) (2005).
18. R. Huber, B. A. Schmid, Y. R. Shen, D. S. Chemla, and R. A. Kaindl, Phys. Rev. Lett. **96**, 017402 (2006).
19. M. Born and E. Wolf, Principles of Optics (Pergamon Press, New York, 1980).
20. For a review see, e.g., B. Ferguson and X.-C. Zhang, Nat. Mater. 1, **26** (2002) and references therein.
21. R. A. Kaindl, et al., Opt. Lett. **23**, 861-863 (1998); R. A. Kaindl, F. Eickemeyer, M Woerner, and T. Elsaesser, Appl. Phys. Lett. **75**, 1060 (1999).

22. R. Huber, A. Brodschelm, F. Tauser, and A. Leitenstorfer, Appl. Phys. Lett. **76**, 3191 (2000)).

23. C. Kübler, R. Huber, S. Tübel and A. Leitenstorfer, Appl. Phys. Lett. **85**, 3360 (2004).

24. T. Zentgraf, R. Huber, N. C. Nielsen, D. S. Chemla, and R. Kaindl, Opt. Expr. **15**, 5775 (2007).

25. F. Eickemeyer, R. A. Kaindl, M. Woerner, T. Elsaesser, and A.M. Weiner, Opt. Lett. **25**, 1472 (2000).

26. T. Bartel, P. Gaal, K. Reimann, M. Woerner, and T. Elsaesser, Opt. Lett. **30**, 2805 (2005).

27. Ch. Fattinger, and D. Grischkowsky, Appl. Phys. Lett. **54**, 490 (1989).

28. Q. Wu and X.-C. Zhang, Appl. Phys. Lett. **68**, 1604 (1996).

29. M. C. Beard, G. M. Turner, and C. A. Schmuttenmaer, Phys. Rev. B **62**, 15764 (2000).

30. D. S. Chemla and J. Shah, Nature **411**, 549 (2001).

31. R. A. Kaindl, D. Hägele, M. A. Carnahan, R. Lövenich, and D. S. Chemla (unpublished).

32. see e.g. G. W. Fehrenbach, W. Schäfer, J. Treusch, and R. G. Ulbrich, Phys. Rev. Lett. **49**, 1281 (1982); N Peyghambarian, et al., Phys. Rev. Lett. **53**, 2433 (1984); W. H. Knox, et al., Phys. Rev. Lett. **56**, 1191 (1986); G. Manzke, et al., Phys. Rev. Lett. **80**, 4943 (1998).

33. M. Kira and S. W. Koch, Many-body correlations and excitonic effects in semiconductor spectroscopy, in G. Eden and H. Jelnikova, Progress in Quantum Electronics, Vol. 30 (Elsevier, Amsterdam, 2006).

34. S. Nikitine, J. Phys. Chem. Solids **45**, 949 (1984).

35. M. Kira and S. W. Koch, Phys. Rev. Lett. **93**, 076402 (2004).

36. P. Y. Yu and Y. R. Shen, Phys. Rev. B **17**, 4017 (1978).

37. M. Kubouchi, K. Yoshioka, R. Shimano, A. Mysyrowicz, M. Kuwata-Gonokami, Phys. Rev. Lett. **94**, 016403 (2005).

38. D. Fröhlich, J. Brandt, C. Sandfort, M. Bayer, and H. Stolz, phys. stat. sol. (b) **64**, 2543 (1994); G. Dasbach, et al., Phys. Rev. Lett. **91**, 107401 (2003).

39. C. Uihlein et al., Phys. Rev. B **14**, 1772 (1976).

40. H. A. Bethe and E. E. Salpeter, Quantum Mechanics of One- and Two-Electron Atoms (Academic Press, New York, 1957).

41. Y. R. Shen, The Principles of Nonlinear Optics (Wiley, New York, 2002).

Figure Captions

FIG 1 (a)-(c) Broadband phase-locked THz transients generated via optical rectification and detected by electro-optic sampling in nonlinear optical crystals as follows: (a) emitter and detector: (110)-GaP (d = 200 μm), (b) emitter: GaSe (d = 100 μm), detector: (110)-ZnTe (d = 15 μm), (c) emitter and detector: GaSe (d = 30 μm), data from Ref. [23], (d) corresponding amplitude spectra (i)-(iii) continuously covering the far- and mid-infrared regime. Spectrum (iv) corresponds to a phase-locked pulse generated by phase-matched optical rectification of a 7-fs near-infrared pulse in a $LiIO_3$ element [24].

FIG 2 (a) Near-infrared absorption spectrum of the quantum well sample at T_L = 6 K (solid curve). The pump spectrum (dotted curve) is resonant with the 1s heavy-hole interband line. (b) Photoinduced conductivity $\Delta\sigma_1(\omega)$ and (c) dielectric function change $\Delta\varepsilon_1(\omega)$ for various *e-h* pair densities n in units of $n_0 = 10^{10}$ cm^{-2}. The data are taken at Δt = 2.5 ps. Solid curves: two-fluid model of Eq. (2); dashed curves at $n = 20 \times n_0$: quasi-2D exciton model of Eq. (1). Curves for different densities are equally scaled and vertically shifted.

FIG 3 Fit parameters of the two-component model to the THz response of Fig. 2. (a) Total electron-hole pair density n as function of excitation power. (b) Free carrier density n_{eh} as a function of n. (c) Intra-excitonic level spacing $E_{1s\text{-}2p}$ (filled squares) measured via THz spectroscopy, and density-induced energy shift ΔE_{NIR} (open circles) of the interband

resonance. (d) Filled squares: Full width at half maximum Γ_X of the THz resonance; open circles: FWHM Γ_{NIR} of the near-infrared absorption line. The solid curves are guides to the eye.

FIG 4 (a) Optical absorption spectrum of the Cu_2O crystal studied in this work (T_L = 6 K). Inset: term scheme of yellow exciton series [39]. Dashed curve: typical pump spectrum for resonant 3p excitation (thick upward arrow in inset). Internal exciton transitions from p to s and d states are dipole allowed (solid arrow). (b) and (c): Pump induced changes ΔE_{THz} (black and blue) at Δt = 1 ps and reference THz fields E_{THz} (gray curves, downscaled by 500). Pump spectra are centered (b) in the continuum at 2.206 eV and (c) resonant to the 3p line. Arrow: phase slip by π.

FIG 5 THz response at Δt = 1 ps after excitation of unbound electron-hole pairs and 3p excitons. (a), (c) Changes of refractive index Δn and (b), (d) absorption coefficient $\Delta\alpha$ (solid lines). Dash-dotted curves: Drude response. Dashed lines: model of three oscillators with energies E_1 = 4.5 meV, E_2 = 6.6 meV, and E_3 = 9.5 meV, and relative oscillator strengths as given in the text. The vertical arrow marks the negative absorption change occurring around 6.6 meV. (e) Ultrafast pump-probe dynamics of the induced change of the THz field at various pump energies.

FIG 6 THz generation in Cu_2O: (a) Pump spectrum (solid black line), (b) real-time trace, and (c) normalized power spectrum of the THz transient (FWHM: 1.7 meV). The spectral

width of the pump pulse is set to 12 meV (FWHM). Inset in (c): Term scheme of the underlying quantum process.

FIG 7 Two-dimensional THz emission spectroscopy of intra-excitonic lines in Cu_2O. (a) THz spectra for a series of different pump wavelengths. All spectra are equally scaled and vertically offset to align with the center photon energy of the respective pump on the right hand scale of (b). (b) reproduces the visible absorption spectrum for comparison. The width of each pump spectrum is kept at 12 meV (FWHM). Vertical lines in (a) mark the energy position of prominent intra-excitonic transitions.

FIGURE 1

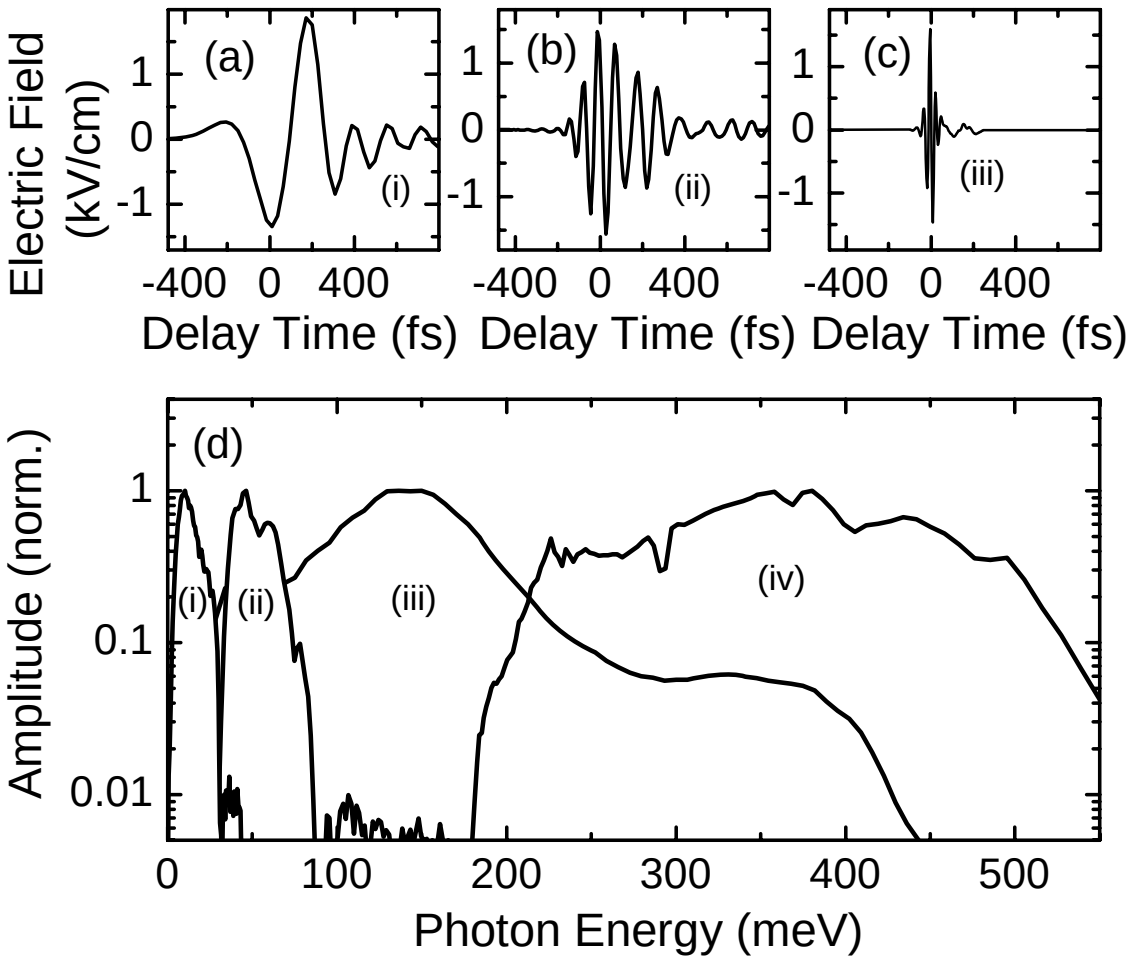
Electric Field (kV/cm)
(a)
(b)
(c)
(i)
(ii)
(iii)
1
0
-1
-400
0
400
Delay Time (fs)
(d)
Amplitude (norm.)
1
0.1
0.01
(i)
(ii)
(iii)
(iv)
0
100
200
300
400
500
Photon Energy (meV)

FIGURE 2

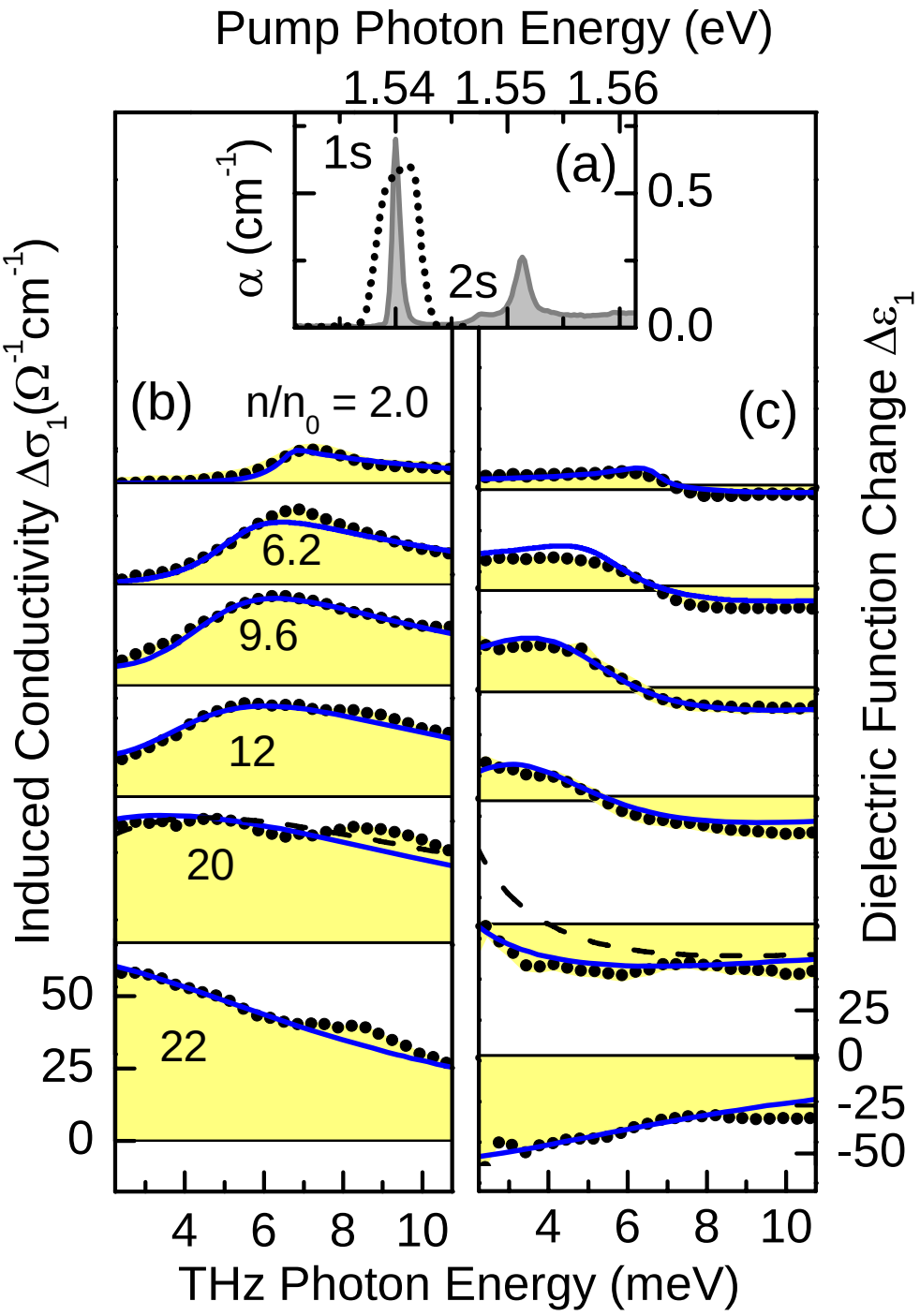
Pump Photon Energy (eV)
1.54 1.55 1.56
1s
2s
(a)
α (cm-1)
0.5
0.0
(b)
n/n0 = 2.0
(c)
6.2
9.6
12
20
22
Induced Conductivity Δσ1(Ω-1cm-1)
Dielectric Function Change Δε1
50
25
0
25
0
-25
-50
4 6 8 10
4 6 8 10
THz Photon Energy (meV)

FIGURE 3

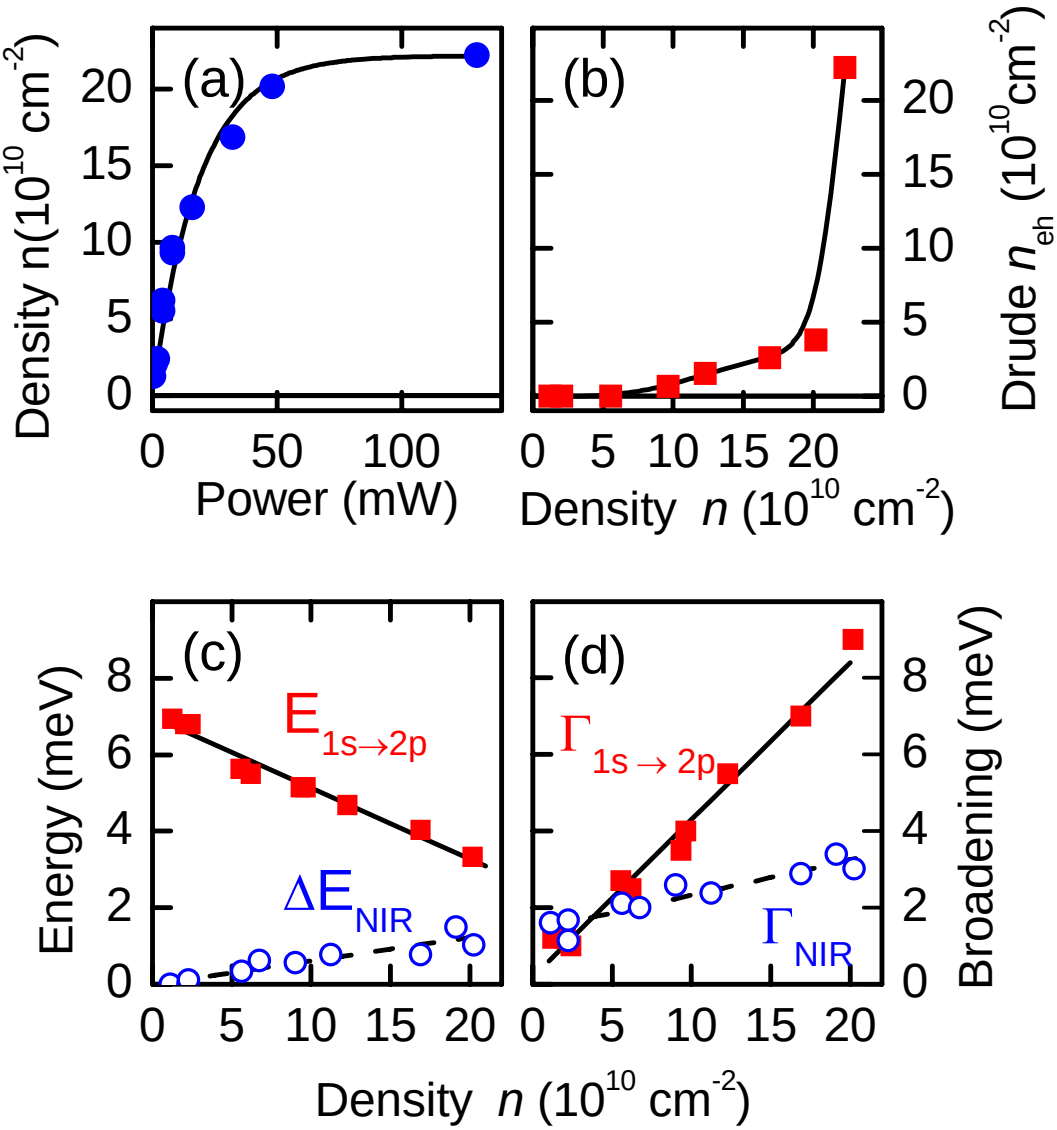
(a)
(b)
(c)
(d)
Density n(10^10 cm^-2)
Power (mW)
Drude n_eh (10^10cm^-2)
Density n (10^10 cm^-2)
Energy (meV)
E_1s→2p
ΔE_NIR
Γ_1s → 2p
Γ_NIR
Broadening (meV)
Density n (10^10 cm^-2)

FIGURE 4

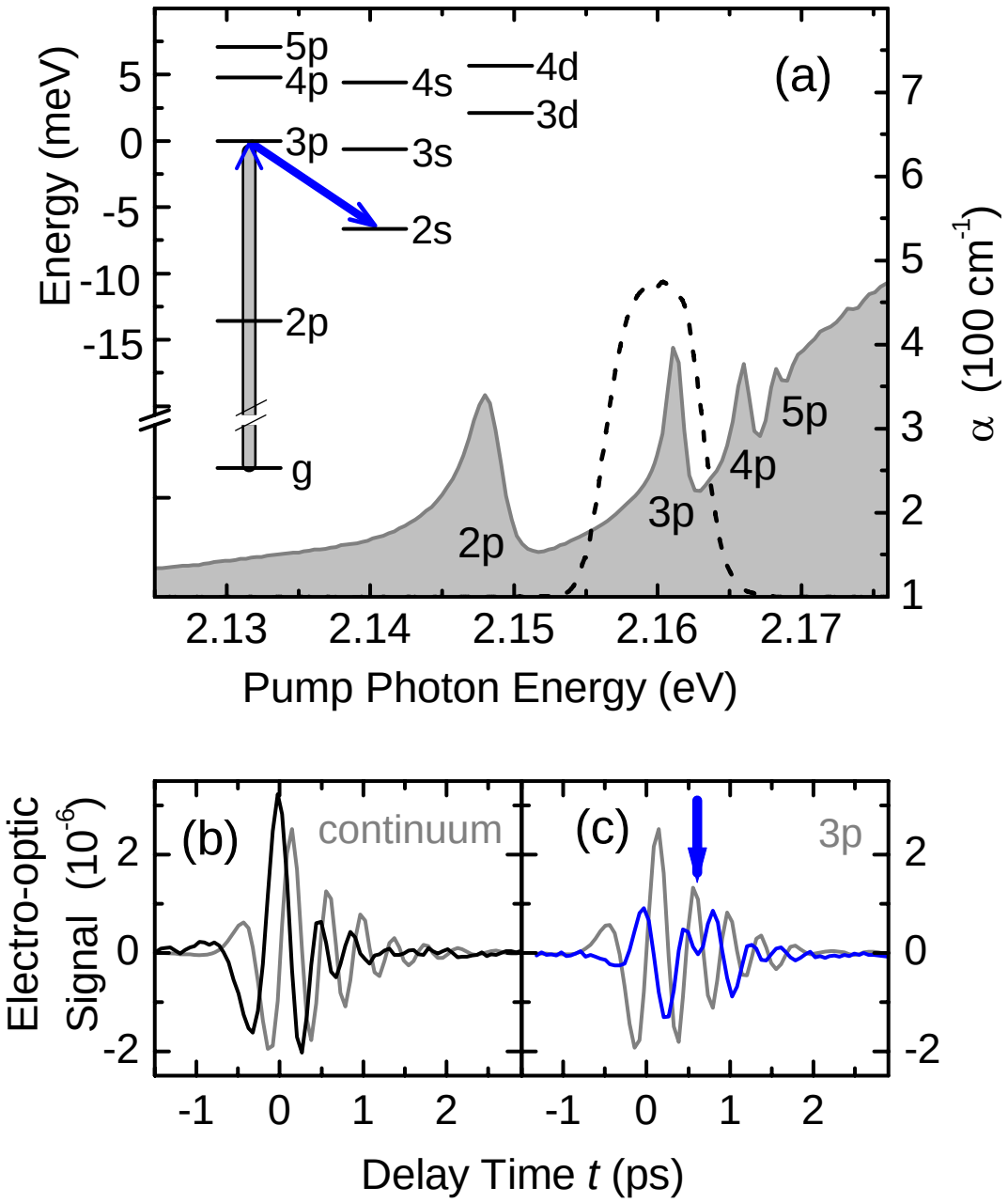
Energy (meV)
5
0
-5
-10
-15
5p
4p
4s
4d
3d
3p
3s
2s
2p
g
(a)
2p
3p
4p
5p
7
6
5
4
3
2
1
α (100 cm-1)
2.13
2.14
2.15
2.16
2.17
Pump Photon Energy (eV)
Electro-optic Signal (10-6)
(b)
continuum
(c)
3p
2
0
-2
-1
0
1
2
Delay Time t (ps)

FIGURE 5

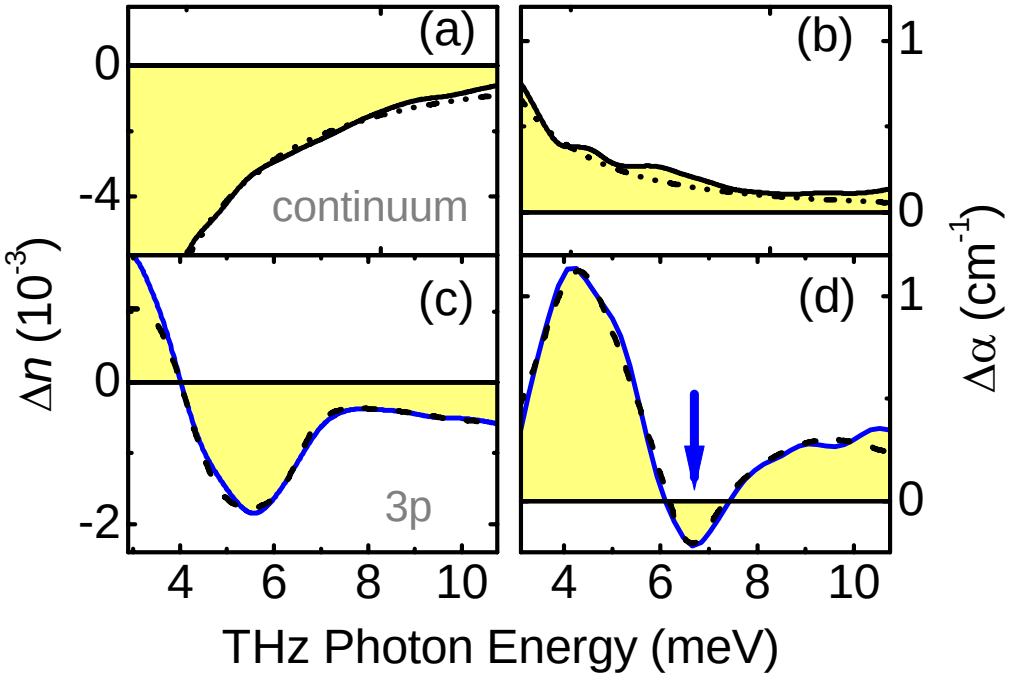
(a)
(b)
(c)
(d)
continuum
3p
0
-4
-2
1
4
6
8
10
Δn (10^-3)
Δα (cm^-1)
THz Photon Energy (meV)

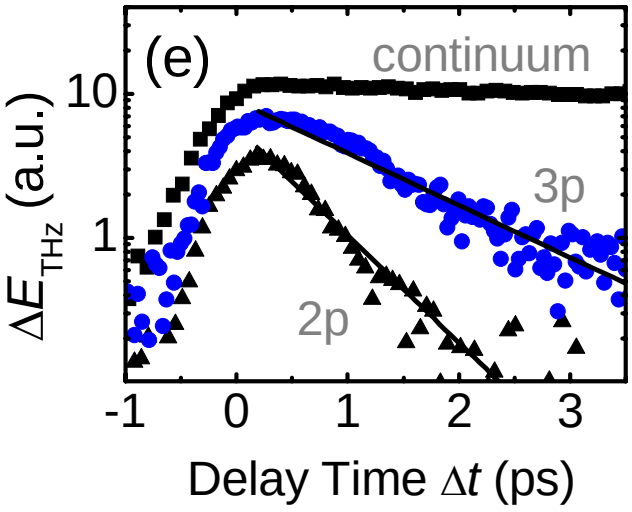
(e)
continuum
3p
2p
10
1
-1
0
1
2
3
ΔE_THz (a.u.)
Delay Time Δt (ps)

FIGURE 6

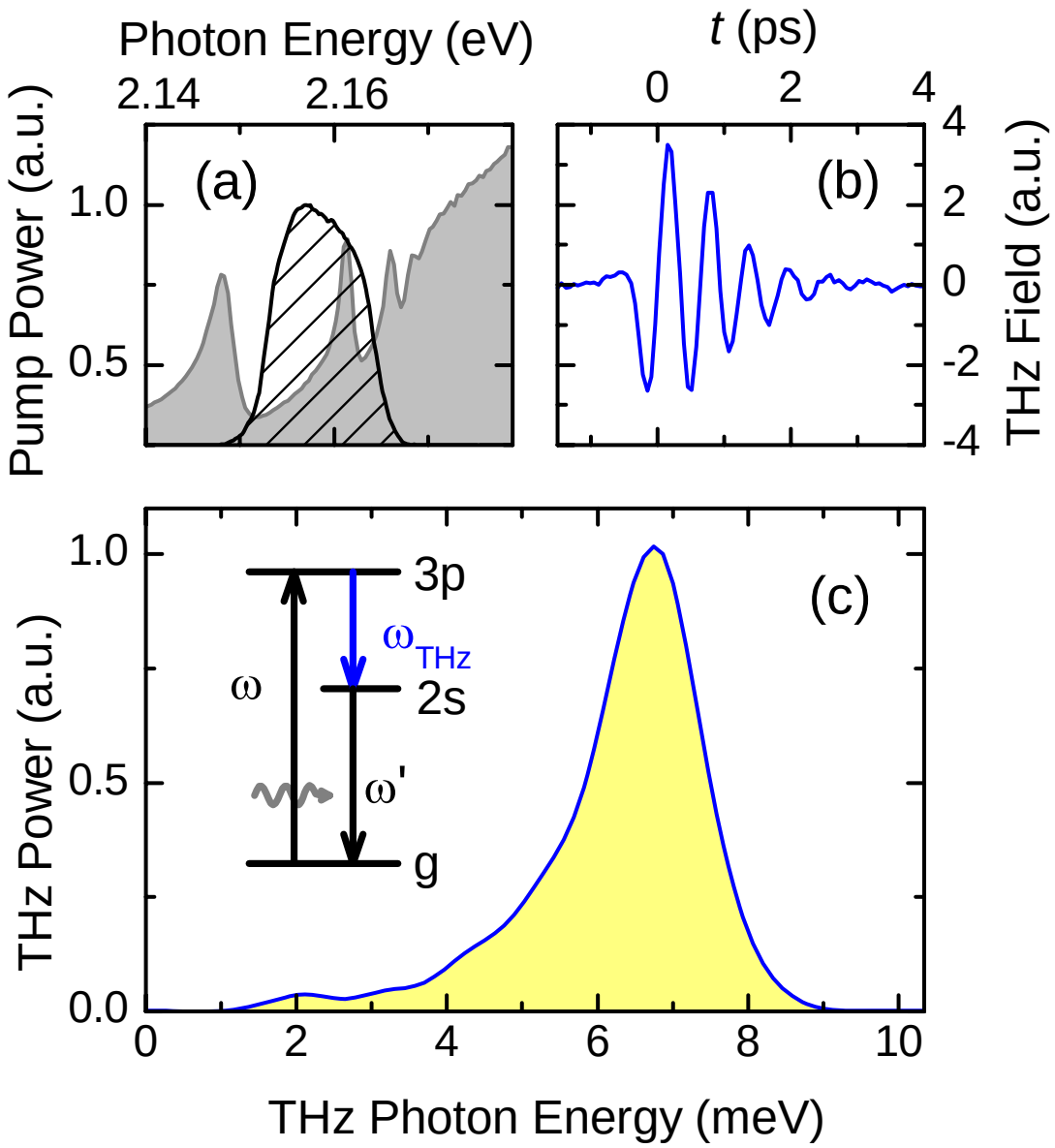
Photon Energy (eV)
2.14
2.16
Pump Power (a.u.)
1.0
0.5
(a)
t (ps)
0
2
4
(b)
4
2
0
-2
-4
THz Field (a.u.)
THz Power (a.u.)
1.0
0.5
0.0
3p
ω_THz
2s
ω
ω'
g
(c)
0
2
4
6
8
10
THz Photon Energy (meV)

FIGURE 7

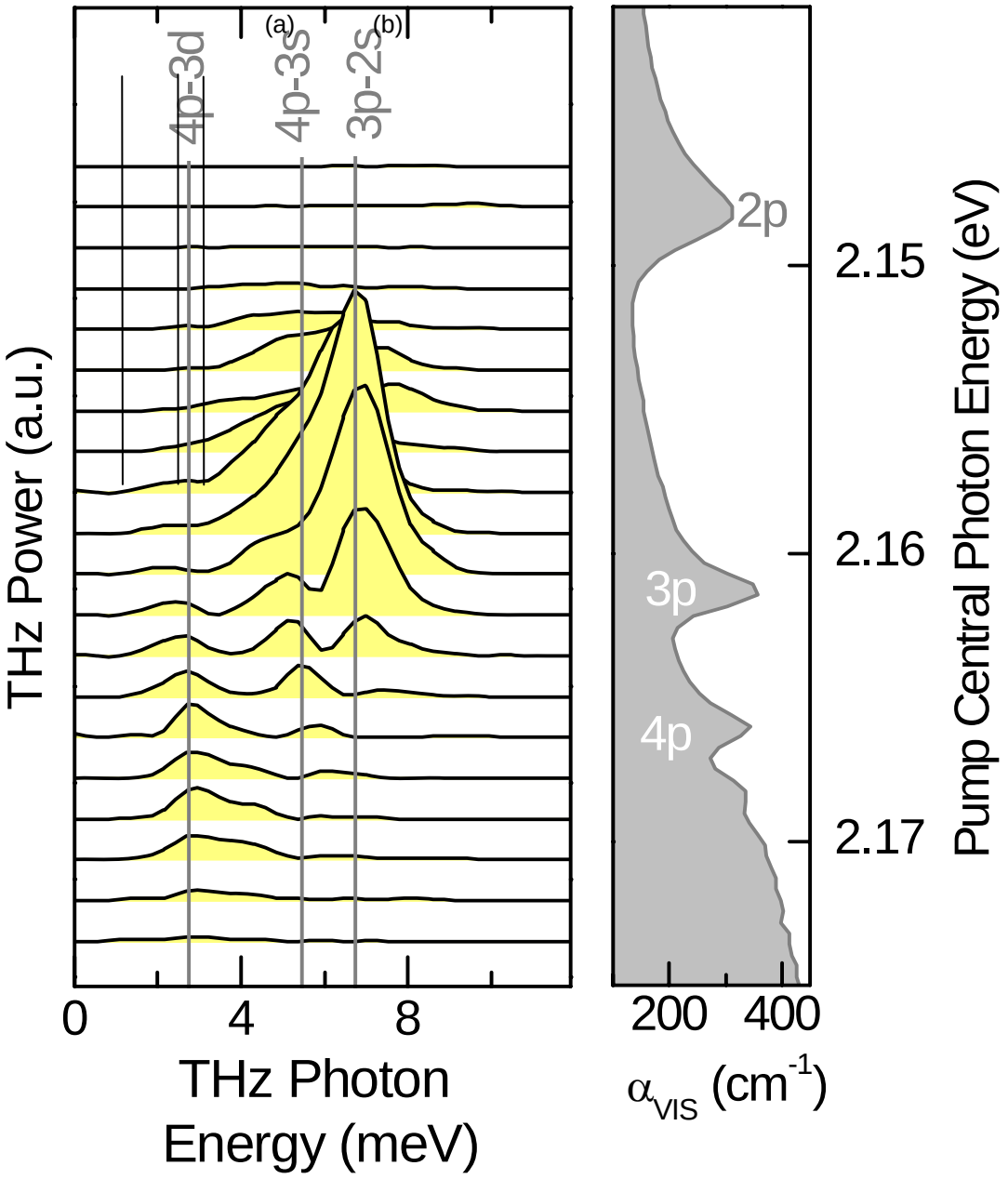
(a)
(b)
4p-3d
4p-3s
3p-2s
THz Power (a.u.)
0
4
8
THz Photon Energy (meV)
2p
3p
4p
200
400
α_{VIS} (cm^{-1})
2.15
2.16
2.17
Pump Central Photon Energy (eV)

DISCLAIMER